Divergent convective outflow in ICON deep convection-permitting and parameterised deep convection simulations

Edward Groot[1], Patrick Kuntze[1], Annette Miltenberger[1], and Holger Tost[1]

[1]Institut für Physik der Atmosphäre, Johannes Gutenberg Universität, Johannes-Joachim-Becher-Weg 21, Mainz, Germany

Correspondence: Edward Groot (egroot@uni-mainz.de)

Abstract. Upper-tropospheric deep convective outflows during an event on 10th-11th of June 2019 over Central Europe are analysed from simulation output of the operational numerical weather prediction model ICON. Both, a parameterised and an explicit representation of deep convective systems are studied. Near-linear response of deep convective outflow strength to net latent heating is found for parameterised convection, while coherent patterns in variability are found in convection-permitting

5   simulations at 1 km horizontal grid spacing. Furthermore, three hypotheses on factors that may affect the magnitude of the convective outflow are tested in the convection-permitting configuration: organisation of convection through dimensionality of the systems, organisation of convection through aggregation and convective momentum transport.

Convective organisation and aggregation induce a non-linear increase in the magnitude of deep convective outflows with increasing net latent heating, as shown by the confidence interval of the best fit between power transformed net latent heating and detected magnitude of outflows. However, mixed and weaker than expected signals are found in an attempt to detect

10   the representation of dimensionality of the convection and its consequences for the divergent outflows with an ellipse fitting algorithm that describes the elongation of the intense (convective) precipitation systems. As opposed to expectations, convective momentum transport is identified to slightly increase the magnitude of divergent outflows in this case study.

1 Introduction

Flow variability may be defined as the evolution of differences in the horizontal winds originating from initial condition uncer-

15   tainty in a model ensemble. However, it may also be defined as the analysis of a specific flow characteristic of a distribution with respect to its median or mean. Lorenz derived expressions for difference evolution of a flow (Lorenz, 1969) in his fundamental research on predictability of atmospheric dynamics. He also demonstrated growth characteristics of initial condition derived flow variability towards the climatological distribution (i.e. the second possible definition). In this century, predictability, meaning flow variability from the initial condition perspective, and its representation in numerical weather prediction (NWP) models

20   have been further investigated (e.g. Zhang et al., 2007; Baumgart et al., 2019).

Flow variability can manifest at many different scales in atmospheric dynamics: from the smallest dissipative scales to planetary Rossby waves. In this study flow variability of mesoscale convection is assessed with the ICON numerical weather prediction model, which represents a state-of-the-art operational forecasting and research model (Zängl et al., 2015; Giorgetta

25 et al., 2018). In particular, the structure of divergent outflow variability induced by deep convection is examined. The role of convective organisation and dependence on precipitation rate will be assessed, based on hypotheses formulated

– following a study of Large Eddy Simulations (Groot and Tost, 2022) ,

– and consistent with previous idealised models (Bretherton and Smolarkiewicz, 1989; Nicholls et al., 1991; Mapes, 1993).

The understanding of convective outflows in Groot and Tost (2022) builds mainly on Bretherton and Smolarkiewicz (1989):
30 based on their linearised gravity wave adjustment model an idealised expression of outflow strength from deep convection was constructed (Nicholls et al., 1991). Therein, deep convection is approximated by a localised heating source. The outflow depends linearly on the net latent heating, if the geometry of the heating source is prescribed. But the slope of the dependency differs between line sources and point sources of heating. Mapes (1993) investigates the consequences of the gravity wave adjustment conceptually for convective organisation: gravity wave activity may facilitate convective aggregation, which was
35 suggested to affect outflow dimensionality by Groot and Tost (2022). Consequentially, outflows from real convective systems conceptually tend to organise into a mixture of idealised point ("3D") and idealised line ("2D") sources. In contrast to the results of Mapes (1993) and Mapes and Houze (1995), who found a reduction of the ratio of mass divergence to net latent heating caused by a stratiform heating influence compared to purely convective heating profile, the LES simulations of Groot and Tost (2022) do not exhibit such behaviour; probably because of an only very weak stratiform contribution to the precipitation
40 systems.

A major step forward in the analysis of the evolution of flow perturbations in this centruy has been achieved from a atmospheric dynamics point of view. A strong (initial) connection of variability growth with (convective) precipitating systems has become obvious (e.g. Zhang, 2005; Zhang et al., 2007; Selz and Craig, 2015a, b). With the help of the potential vorticity perspective, narrow initial condition spread could reveal this link directly (Selz et al., 2022; Baumgart et al., 2019; Rodwell et al., 2013).
45 However, such cases are from a practical perspective currently improbable due to the mostly larger initial state uncertainty. Nevertheless, this uncertainty will pertain and propagate in all situations. It introduces the growth of flow perturbations due to scale interactions (which may cascade both upscale and downscale in practice (Lorenz, 1969; Durran and Gingrich, 2014)). Despite, improvements can be utilised to further reduce uncertainty on small scales (Selz et al., 2022; Zhang et al., 2019).

Baumgart et al. (2019) have investigated the sequence of dynamical processes that (on average) contribute to mid-latitude
50 growth of flow perturbations. They proposed that latent heating tendencies from their deep convection scheme in ICON may induce differential divergent winds in the upper troposphere. Subsequently, further non-linear growth of flow perturbations in the upper troposphere is driven by differential advection. A key question is whether the variability in flow perturbations is comparably (and reliably) represented in simulations with resolved and parameterised deep convection. A latent heating conditional perspective on convectively induced flow variability is taken in this study. The analysis from the conditional perspective will be
55 compared to results obtained with an LES-model and the consistent idealised gravity wave outflow magnitude (Groot and Tost, 2022; Nicholls et al., 1991). Furthermore, indirectly, a pathway via which organised convection could play a role in processes of perturbation growth may be identified. This role of organised convection for flow perturbations has been suggested by e.g., Rodwell et al. (2013) and Clarke et al. (2019b, a).

Furthermore, convective momentum transport (CMT) can modify upper-tropospheric flow perturbations induced by deep con-
vection (Rodwell et al., 2013). Rodwell et al. (2013) found that mesoscale convective systems over the North-American con-
tinent could affect European weather predictability. CMT may not only play a crucial role in the organisation of convective
systems, but also in downstream perturbation development. Groot and Tost (2022) noted that the effect of CMT could be sep-
arated into a direct and an indirect effect: firstly, CMT affects divergent flow and associated horizontal acceleration directly,
resulting in flow perturbations around convective systems. Secondly, as CMT affects the convective organisation and precip-
itation rates, this results in an indirect modification of upper-tropospheric flow. A direct effect on divergent outflows was not
identified in LES (Groot and Tost, 2022), possibly due to too weak upper-tropospheric shear. In this study, the direct effect of
CMT on divergent outflows from deep convection will be assessed for ICON simulations.

The missing - but crucial - modelling strategies that complement idealised models like the linearised model and idealised LES,
from which physical understanding of processes could be gained, will be examined in this study. Bridging the gap to opera-
tional NWP (ICON 2.6) is a step towards a (very) basic understanding of divergent deep convective outflow magnitudes across
a broad range of simulation set-ups. Meanwhile, the relationship between net latent heating and divergent convective outflows
in the upper troposphere is assessed in a realistic, but also complex setting. Both parameterised and explicitly resolved deep
convection are used: thereby, potential limitations of the parameterised treatment of deep convection may be exposed. In Groot
and Tost (2022) a linear relation of outflow strength to net latent heating was found, with superposed variability induced by
outflow dimensionality.

Altogether, the following (LES-inherited) hypotheses will be tested on convection-permitting ICON simulations:

- The dimensionality of convective systems substantially affects the magnitude of divergent outflows. In case of divergent
  outflow from isolated convective cells compared to the outflow of convection closely resembling a line source of heating
  (e.g. elongated squall lines), a contrast in ratio between divergence and latent heating is expected: at the same area mean
  intensity of latent heating, less divergence is expected for a linear geometry than for a corresponding point source.

- Convective aggregation and organisation affects the magnitude of divergent outflows - the outflow is expected to increase
  at a rate slower than linearly when convective aggregation leads to increases in the mean precipitation rate (probably
  partly explained by adjusting the outflow dimensionality).

- CMT does not affect the magnitude of divergent outflows from deep convection and hence normalised convective mo-
  mentum transport does not have a statistically significant relation with the normalised ratio between mass divergence
  and precipitation rate.

To assess the above hypotheses, convective systems are tracked in convection-permitting ICON. The relationship between net
latent heating and the magnitude of divergent outflow from deep convection in the upper troposphere is evaluated based on
the findings by Groot and Tost (2022). Hypotheses are tested using an ellipse fitting algorithm to assess the elongation of
convective systems (a concept used before by Grant et al. (2020) and references herein), with validation procedures to as-
sure consistent parameter evolution. Furthermore, convective systems that resemble an elongated squall line are examined in

convection-permitting simulations. Squall lines resemble line sources of heating better than other convection. In the param-
eterised convection set-up variables are integrated over a box volume in various simulations, with a set-up similar to Groot
and Tost (2022). Hereby, it is chosen to not track the systems. Diagnostics are integrated over a one hour window for each
95   convective system instead (motivated in Section 3.2.2).

The manuscript is organised as follows: after a short synoptic discussion of the simulated case (Section 2), the model and simu-
lation configuration is described in Section 3, including an example track of a convective system and corresponding evolution of
the parameters of an ellipse fitting algorithm (Section 4). Then, the upper-tropospheric (250 hPa) divergence variability among
convective systems in parameterised convection and convection-permitting ensembles is assessed in relation to the location of
100   convective features in Section 5.1. Subsequently, the divergent outflows are compared between parameterised convection and
convection-permitting simulations (Section 5.2). This is followed by an assessment of the three hypotheses presented above in
Section 6 for convection-permitting simulations. Subsequently, a synthesis and discussion section is presented (Section 7).

2   Synoptic conditions of the case study

The organised convection over Central Europe on June 10th and 11th is notorious for the Munich Hail Storm (Wilhelm et al.,
105   2021). An upper-tropospheric low pressure system was located over Western France on June 10th 2019 (Figure 1; grey isolines
with geopotential height patterns), with a southerly flow advecting warm, moist air northward over Central-Europe (high θ_e,
red). The associated pattern with cold air west of the upper low pressure system led to strong baroclinicity over France, the
Alps and (later) Germany. Cold surface air creeping northeastward directly ahead of the collocated cold front supported the
initiation of strong convective systems. These systems are present in nearly all simulations, albeit at slightly different locations
110   than in reality, including east of the front in the region of warm near-surface air. Storms generally appeared further to the west
in the convection-permitting ensemble and even more so in the parameterised set-up than in reality.

After all, several systems with mesoscale convective activity developed over Germany and the Alps during the afternoon and
evening, which were co-located within the parameterised deep convection ensemble. Similarly, convection was relatively ac-
tive in convection-permitting simulations over Southern-Germany in the (late) afternoon of the 10th of June (e.g. Figure 5a;
115   observed convective systems are also shown there). Well organised convection occurred over regions with strong relief in the
southwest. In the east initially surface-based convection occurred in the late afternoon to early evening. The strong south to
southwesterly upper-level flow helped to organise convection in convection-permitting simulations to a varying degree: a few
convective systems in the east of Southern-Germany developed squall line-like structures. On the contrary, other structures
only organised into smaller multicells. This mixture may be very suitable for assessments of divergent outflows from deep
120   convection, since idealised LES simulations suggest that convective organisation, geometry and aggregation may be crucial
aspects for the outflow. These aspects determine the normalised outflow strength with respect to net latent heating (Groot and
Tost, 2022). A more detailed discussion of the synoptic configuration and actual convective evolution around this event is
provided in Wilhelm et al. (2021) .

Figure 1. Equivalent potential temperature at 600 hPa (blue-white-red), isotachs at 250 hPa (30 to 60+ m/s at 5 m/s intervals, transparent colors) and geometric height of the 250 hPa surface at ca. 11 km height and with 50 m intervals forecasted for 22 UTC on June 10th over Western Europe.

3 Methods

3.1 Model set-up

3.1.1 Domains, grids and parameterizations

This study investigates numerical simulations with ICON 2.6 (Zängl et al., 2015; Giorgetta et al., 2018), which is developed and operated by the German Weather Service and Max Planck Institute for Meteorology. Simulations have been conducted and analysed in the following configurations:

- Global simulations, with a nest over Europe ("PAR")

- Convection-permitting simulations over Southern-Germany ("PER") using the local area mode (LAM)

The PAR-simulations have been initiated at 12 UTC on June 10th 2019, whereas PER-simulations over Southern Germany have been initiated at 03 UTC (Figure S1 in the Supplement). For details on simulation settings, see Table 1. We refer to Prill et al. (2020) for the mostly similar default parameterisation settings.

Table 1. Simulation settings within the three domains.

Domain	Global domain	European Nest	LAM, Southern Germany
Model version	2.6.0		2.6.2.2
Grid spacing (km)	26 (R03B06)	13 (R03B07)	1 (R05B09)
Time step (s)	100	50	10
Domain top altitude (km)	75		22.5
Number of vertical levels (-)	90		90
Deep convection parameterisation	Tiedtke (1989), Bechtold et al. (2014)		None
Time step deep convection (s) and subgrid orography	1200	600	
Time step gravity wave drag (s)	1200		
Microphysics parameterisation	1M (Seifert, 2008)		2M (Seifert and Beheng, 2006)
Radiation parameterisation	Ritter-Geleyn[1]		RRTMG
Time step radiation (s)	1800		600
Grid spacing radiation (km)	52	26	1
Rayleigh damping height (km)	22		12.5
Initial conditions	DWD analysis		KENDA, provided by Matsunobu et al. (2022)
Initial condition time	12 UTC		03 UTC
Initial condition set	Deterministic		20 member ensemble
Ensemble perturbations	Surface dataset ($n = 6$; 2015-2018)		Initial conditions
Boundary conditions	None (two-way nested)		ICON EU ensemble forecasts (20 km)
Additional perturbed simulations (number)	Rescaled: - Latent heating $\pm5\%,\pm10\%,\pm20\%$ (6) - CMT tendencies (none, $\pm50\%$) (3) Deep convection scheme: - No parameterisation (6, ensemble perturbations) - Adjusted calling frequency (2)		None
Output time step (min)	None	10	5
Total integration time (hours)	33		16

135

3.1.2 Ensemble and perturbation settings

Ensembles have been used with the aim to sample an unspecific form of background convective variability within a similar large-scale flow configuration. To further sample the variability, experiments with adjustments to the default PAR-set-up have been done, essentially matching Groot and Tost (2022) (Table 1). Global nested simulations have been perturbed with alternative surface tile dataset, whereas the 20 member initial condition ensemble closely resembles the operational ICON D2-ensemble of DWD.

The combined variability imposed by selecting various convective systems over a time range and through the dimension of ensemble members allow us to study the characteristics of convective variability in a precipitation-conditional framework.

The results presented will mostly be focused on the comparison of the PAR and PER ensemble and on the PER ensemble itself.

3.2 Extracting convective system properties in ICON simulations

Extraction of convective system properties (shape, area, etc) can be achieved in the PER-simulations. On the contrary, parameterised treatment does not lend itself very well to such an extraction procedure, because it assumes that a statistically averaged effect of convection over larger scales exists and is represented (e.g. Done et al., 2006) . Therefore, any description of (sub-grid) variability induced by convective cells and convective organisation is represented less accurately than in convection-permitting simulations with finer grid (if at all represented). The extraction procedure of organised convective systems and associated metrics from the PER-simulations is described in section 3.2.1, followed by discussion of metrics from PAR in 3.2.2.

3.2.1 Convection-permitting simulations "PER"

It is important that the dataset with properties of convective systems is able to describe the degree of convective aggregation, orientation and the relative state of elongation in time and space (similar to a dimensionless number). Consequently, it is possible to single out whether an almost 2D- or almost 3D-outflow regime can be expected . These factors have been found to determine the relative magnitude of outflow from deep convection (Groot and Tost, 2022) . To estimate parameters describing the elongation and state of aggregation for any convective system, an ellipse fitting algorithm has been designed. In parallel, an independent moving box is initiated to track a convective system. The independent box is needed to conserve a moving integration volume, relative to the convective system's main updraft, over which divergence and precipitation are integrated. The following steps lead to a dataset of convective systems and ellipse parameters:

1. Ellipse fitting

2. Validation of obtained ellipse parameters

3. Construction of precipitation rate, filtered mass divergence and convective momentum transport diagnostics

4. Moving box integration of the constructed diagnostics along a convective system's track

5. Matching between ellipse parameters and moving box diagnostics

6. Final check of the matched records

The full procedure is explained below.

170 Ellipse fitting is applied to any area larger than about 400 km^2 with a precipitation rate over 10 mm/h in PER-simulations. Before fitting the ellipses, a binary representation of convective precipitation is smoothed spatially ($\sqrt{r}$ dependence) over a 20 km radius. Subsequently, an initial validation procedure assesses the stability of the ellipse parameters over a one hour window. Short lasting very strong fluctuations are filtered out. Only fluctuations that match any prior and successive record within one hour are maintained (Groot and Kuntze, 2023). Note that the corresponding prior or successive records might have been

175 incidentally removed by this procedure. Removal of each independent record is possible: at least one plausible predecessor and successor of each validated record has to exists in this step, both forward and backward in time. Additional validation measures check the distance between an ellipse center (set to be < 20 km) and a convective system's track, identified with an independently moving box. A list of ellipse parameters extracted in the procedure is provided Table A1 (Appendix).

Independently from ellipses, a moving box has been initiated subjectively and moves with a convective system. The box is

180 used for integration of precipitation and divergence over a horizontal subspace that is constant in time (with respect to the moving box centre). The convective systems propagate with relatively constant velocity north- or northeastward and only 1-3 systems have been tracked in each simulation (see also Figure 5.1). Manually defined boxes moving at a constant velocity could therefore be used to define the box outlines. The moving boxes are initiated and then track the systems independently from the ellipse fitting procedure, because merging events (such as between smaller satellite ellipses and larger ellipses) occur frequently

185 in the ellipse dataset. In case of a merging event, ellipse parameters will weakly vary in time, but the spatial integration mask of the moving box should not change accordingly. If ellipse parameters vary strongly, the validation procedure is not passed. The signal of divergence and precipitation within a box should predominantly be affected by the main, central convective system within the box and only be weakly affected by satellite systems that develop from time to time around some of the systems.

For each box and time step the following variables are calculated: Firstly, the strength of convective momentum transport

190 (CMT) is computed to determine whether and how this acceleration (deceleration) affects the upper-tropospheric divergence. The estimate of CMT is based on the eddy covariance of perturbations (') in u, v, w from the domain mean values. Separate estimates of the meridional and zonal correlations with vertical velocity representing (resolved, vertically integrated) convective momentum transport fluxes are made at model level 25: located at 315 hPa or about 9 km altitude. This level is selected, because the eddy flux in the upper troposphere turns out to be mostly maximal at or near this level during the studied event.

195 The box mean values of $u'w'$ and $v'w'$ represent the vertical integral of CMT acceleration over all levels below. Both CMT and divergence are normalised with respect to mean surface precipitation, i.e. a proxy of box mean latent heating (into quantities called C and D), to investigate the connection between anomalies in both quantities (conditioned on precipitation rate) in a more robust way. Secondly, the mean precipitation intensity and the filtered mean divergence (wavelengths > 45 km in both horizontal directions, variability at short wavelengths removed) is computed. These three quantities can only be computed

200 if the whole box lies within the extent of the simulation output at any given time. Finally, the ellipse characteristics of the

ellipses contained within each box (elongation A: length ratio between two ellipse axes; O orientation; area of the ellipses) are then matched with the corresponding records averaged over the moving box. An example of the path of a moving box and (contained) ellipses with corresponding ellipse parameters for one convective system is provided in Section 4.

The ellipse dataset fulfilling all conditions of quality control contains 456 records, in which the time evolution of 22 of a total of
205 28 convective systems is represented. This dataset is the basic dataset for the assessment in Sections 5.2 and 6. With a slightly weaker box-center-to-ellipse-center distance criterion, a second dataset of 866 records is obtained. For this larger dataset, the distance criterion was set individually for each convective system (based on e.g. box size) or replaced with an ellipse area criterion. In the larger dataset, all 28 convective systems are present. Since the validation algorithms turned out not to be fully failsafe, ambiguous records have manually been selected before finalising both datasets: 5 additional matches were ambiguous
210 (duplicates fulfill all validation criteria at one specific time stamp) in the dataset of 866 (+5) and 2 of those occurred in the dataset of 456 (+2) records. The double matches among those ambiguous records were manually selected (removed) based on area and centre location of the ellipse.

3.2.2 Convection parameterising simulations "PAR"

In past times, computationally feasible NWP resolutions required the application of a parameterisation to represent deep con-
215 vection. Only recently, global convection-permitting simulations have been utilised for research purposes (e.g. Judt, 2020) . The philosophy behind the representation of deep convection is and has been generally different between parameterised convection and convection-permitting simulations approaches - for simulations with parameterised deep convection:

- Convective cells are not advected with the background flow, but have their full life cycle within a cell: there is a split between dynamics and the parameterisations in each grid cell (Lawrence and Salzmann, 2008; Prill et al., 2020)

220 - An equilibrium assumption is done (e.g. Done et al., 2006) , where (deep) convection represents the adjustment mechanism of the atmosphere to the presence of static instability. Adjustment occurs under the condition that convection can be triggered. Grid cells in numerical models are so small nowadays that the equilibrium, between convective forcing and the adjustment on a separated scale, is questionable.

As a consequence, the representation of deep convection by parameterisation does not only tend to smoothen precipitation
225 through its coarser resolution, but also through underestimated spatial variability (Keane et al., 2014) . Even though there is small differences between the assumptions applicable to different convection schemes (Arakawa, 2004) , arguments above and the comparatively large grid size imply that convective organisation is not directly represented in simulation set-ups with parameterised deep convection. Categorisation through convective organisation is poorly (if at all) justifiable (see also Satoh et al., 2019). Consequently, application of a complex tracking algorithm following parameterised deep con-
230 vective systems is not suitable. A statistical sample of convective cells technically regenerates anyway, while a corresponding precipitation displaces itself over a conditionally unstable or lifted air mass. Furthermore, the LAM-domain is small (400 by 500 km), whereas the parameterised convection simulations cover Europe. A typical (mesoscale) convective system is easily contained within a box of several to tens of grid cells in each horizontal direction for ICON-PAR. Therefore, three static

boxes are chosen and compared among the PAR-simulations. These boxes are set-up such that the dominant precipitation and
divergence signals associated with convective systems fall within the boxes, as needed. Three very different deep convective
systems are systematically compared across six ensemble members.

4   Example of a track in ICON-PER

The track of one of the two convective systems in ensemble member 14 of the PER simulations is illustrated in Figure 2a. The
box centre is indicated as a red line, with bi-hourly markers along the way. The first snapshot at 12:30 UTC shows that the
ellipse algorithm detects an aggregated convective system at the edge of the box. This large system does not fully fall into the
box. The validation procedure automatically reports a failure (represented by an X) because of a too large distance between the
box centre and the convective system.

Subsequently, small convective cells develop near the center of the box (14:30 UTC). The easternmost system obtains a sur-
rounding ellipse located within close range of the box centre. Another one to the west also obtains an ellipse, but the distance
to the box centre is larger. Therefore the latter match is rejected.

Two hours later, again two matches are found: one very near the box centre and one to the north of the centre, but within the
box. The larger central one matches through the distance rule, but the northern one gets rejected.

At 18:30 UTC, an elongated convective system develops in association with the earlier central system (14:30, 16:30 UTC).
Still sitting close to the box centre, it is the only ellipse within the box.

In Figure 2b the evolution of the ellipses over short time intervals is illustrated. The differently colored precipitation and
box features move to the northeast slowly. However, the ellipses undergo various changes, which is associated with a slight
convective reorganisation. The reorganisation is induced by new cell formation in a close proximity of the older system. The
northeastern feature is detected throughout, but blue crosses demonstrate that the match is initially rejected. The box is slowly
closing in on the system, as revealed by the possible match (square marker) at the sixth and last time step. For the southwestern
system, the initial system (larger purple ellipse associated with it) breaks up into smaller pieces for two successive time steps
and eventually disappears. One of the ellipses of the southwestern system (blue circle) matches with the box at one instance
(green), when the ellipse is closest to the box centre.

However, the northeastern system matches at just one instance: the last time step. This match is only valid for the larger dataset
with relaxed conditions. This illustrates how convective (re-)initiation and small displacements can affect the ellipse parame-
ters. Corresponding jumps in evolution of ellipse parameters are filtered out. The wobbly interval is indicated by the dark red
outline at 17:30-18:00 UTC. Most ellipses in this interval are rejected due to such behavior, but some are retained during the
interval. A temporary shrinking in the axes is seen (without consequent rejection in the validation), due to the stability criteria
and interpolation from any neighbouring records within an hour. Another jump within the time window is seen in the offset
parameters (Figure 3). Nonetheless, the general behavior is mostly smooth over the five hours. The behavior illustrates that the
regenerating systems can successfully be detected, covering its temporal evolution.

The evolution of upper-tropospheric divergence, CMT and precipitation rate over the moving box is found in the supplement

(Figure S3). Around 13 UTC no records of the system are validated: the validation criteria haven not been fulfilled (green solid outline in Figure 3).

Between 14 and 15 UTC two convective systems have been matched with the box (Figure 2). One is travelling at a distance of about 20 grid cells from the box centre and the other at about 4-9 cells (10-20 km).

The distance between the centre of an ellipse and the associated convective box centre is maximum 9 grid cell distances (20 km) for the strict dataset of 456 records (purple line versus pink dashed outline in Figure 3).

5 Intercomparison of divergent convective outflows in ICON-PER and ICON-PAR

5.1 Convective systems and associated patterns in divergence (variability)

Figure 4 depicts the evolution of the vertical profile of horizontal divergence averaged over 28 convective systems in PER, although at no point in the evolution all 28 systems are simultaneously present. The time evolution of the median levels of neutral divergence of the systems is shown by the black dashed lines, with grey dashed lines representing the upper and lower quartiles of the distribution.

Inflow of deep convection predominantly occurs in the boundary layer (931 to 800 hPa mean pressure) initially. Subsequently, the convection tends to become elevated (16-19 UTC) in ICON PER, dominated by inflow at 600-800 hPa.

Furthermore, inflow and entrainment typically occurs up to about 450 hPa. Above this level the main outflow region extends upward. A strong vertical gradient in the mean divergence is found around 180-190 hPa, close to the tropopause. Near to this level, many convective systems have another level of neutral divergence, i.e., the upper boundary of the divergent outflows in ICON-PER.

PAR-profiles also reveal a strong divergence maximum directly underneath the tropopause (see supplementary material: Figure S5). The levels of neutral divergence at the tropopause occur at altitudes similar to those found in explicitly simulated convection. However, the variability of the lower level of zero divergence, between 500 and 350 hPa, is increased when utilising a deep convection parameterisation.

According to Figure 4, the maximum of divergence occurs between 200 and 300 hPa. The spatial variability of horizontal divergence is illustrated in Figure 5 b-d at about 250 hPa (i.e., within the layer of maximum divergence) in ICON-PAR and ICON-PER ensembles, in combination with surface precipitation rate. Figure 5a shows the tracks of 22 of the convective systems passing over southern Germany in PER. These convective systems generally move from southwest to northeast through the domain. As only a subset of the records were validated, straight sections without markers can occur along tracks for rejected ellipses. Few systems move northward (e.g., the initially easternmost system). Generally, the precipitation systems tend to increase their intensity and size with time - correlation coefficients between output time and system intensity area are 0.22, 0.25 respectively (see also Figure 9). While the overall mean precipitation rate over the moving boxes is 3.1 mm/h, the value increases to 4.4 mm/h between 17:30 and 19:00 UTC. Furthermore, the average position of the box centres moves toward the northeastern quadrant of the simulation domain in the last 1.5 hours, which is also the region with the largest ensemble variability in the 255 hPa divergence overall (Figure 5 a). The large variability in the divergence is associated with the proximity

(a)
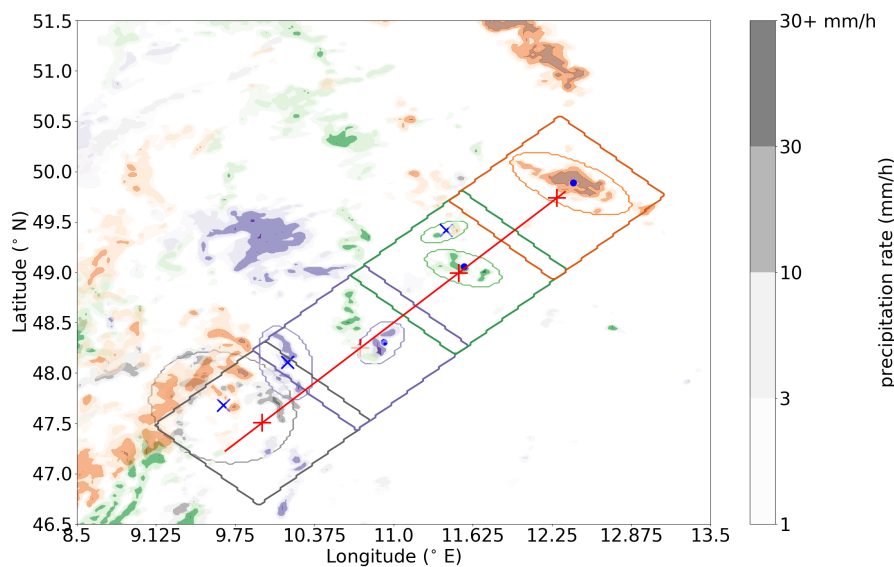
(b)
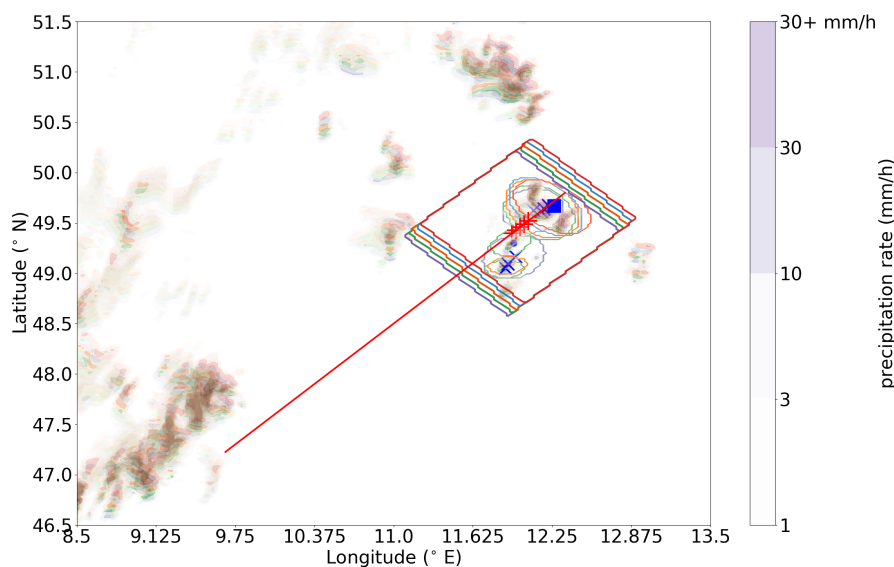
Figure 2. Precipitation rate (mm/h) in ensemble member 14 of the PER simulations at (a) 12:30 UTC (grey color scale), 14:30 UTC (purple), 16:30 UTC (green) and 18:30 UTC (orange). The color intensity represents precipitation rate according to the color bar shown for 12:30 UTC. Ssame for 17:30-17:55 UTC with 5 minute intervals (b). The box outline (tilted rectangles) designed to track the convective system is displayed in the same color. The edges of ellipses matched with the box outline are also indicated. The track of the box with time is indicated by a red line and its centre location is indicated by a +. The distance from that red plus-sign to the ellipse center (blue markers) is evaluated and marked with an x for distances larger than 11 grid cells (about 25 km), a blue circle for those within 20 km and a blue square for those at 20-25 km distance.
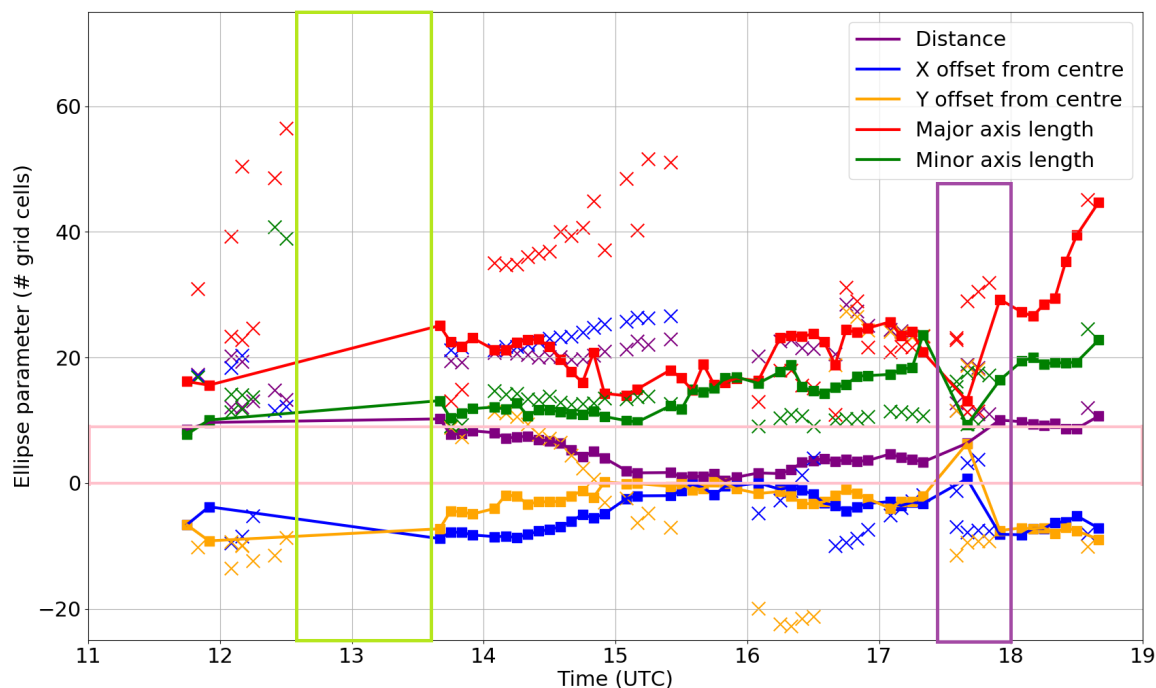
Figure 3. Example of time evolution of ellipse parameters in the dataset for the same convective system as shown in Figure 2, halfway through the validation process. Different colors indicate various ellipse parameters. Red: Major axis length, green: minor axis length, purple: distance from box center (+ in Figure 2); blue and orange: offset in x- and y direction from box center). Crosses represent rejected ellipse records for any of the final datasets. Square markers with a line indicate accepted records. The subset within the pink dashed outline indicates the presence of a record in the small subset of 456 records.

300   of increasingly active convective systems.

Results for PAR simulations are shown in Figure 5c and d for two different simulation time steps: maxima in upper-tropospheric divergence variability are again co-located with enhanced convective precipitation. However, not all regions with (strong) precipitation are directly connected to enhanced upper-tropospheric divergence variability. One possible explanation for a weaker relation may be the release of latent heat substantially below 250 hPa, which would lead to divergence in the middle instead

305   of the upper troposphere. Another reason for weak connectivity are small deviations from the ensemble mean, both in precipitation rate and mass divergence. Furthermore, ensemble mean precipitation rates smoothen spatial maxima of individual members.

In Figure 5 the convective system over the Swiss Alps (9°E, 47°N, panel c) and those over Northern-Central Germany (51°N, 10°E and 53.5°N, 12°E, panel d) are the regions dominating divergence variability. Consequently, rectangular boxes (purple)

310   define the integration mask for the following analysis.
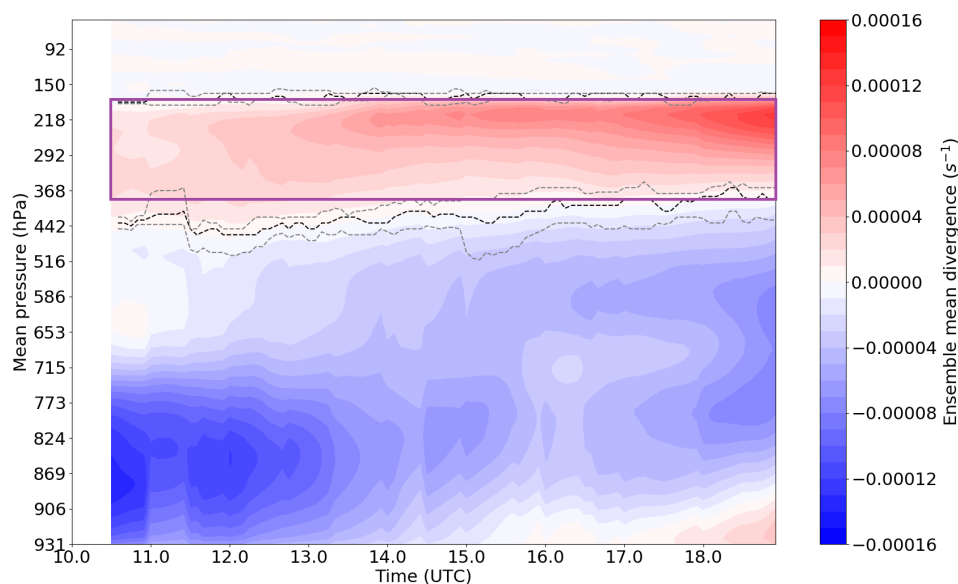
Figure 4. Evolution of mean divergence (convergence) along the track of 28 convective systems as a function of mean pressure. Note that at each instance only a subset of the 28 convective systems will actually be active. Black dashed lines indicate the median level of neutral divergence at any time and grey dashed lines the corresponding 75th and 25th quantiles (nearest to the vertical maximum of divergence). The solid purple outline indicates the levels between which the divergent outflow has been integrated in PER.

5.2 Comparison of relationship between net latent heating and outflow divergence in ICON-PER and ICON-PAR

Figure 6 shows the relation between outflow mass divergence and precipitation rate in all of the analysed ICON-simulations. Records ($n = 456$) with validated ellipses are included (Figure 6a). Furthermore, the evolution of three separate convective systems that eventually develop into squall line-like structures are highlighted by colored symbols (see Figure S5 of the supplement for their distribution of precipitation rate). These systems resemble two-dimensional convection much closer than isolated three-dimensional-like systems. The three colored lines show the precipitation rate and divergence of these three systems in the stage of squall line-like development. Time increases with increasing precipitation intensity (towards the right). Figure 6a shows that, while squall line structures develop (colored lines), D (i.e., normalised divergence) moves towards lower values over time.Consequently, mass divergence becomes comparatively low compared to a fitted mean mass divergence at a given precipitation intensity. The slope between mass divergence and precipitation rate effectively represents the normalised mass divergence, namely D (if the intercept at 0 mm/h is 0 divergence, which is a reasonable assumption for cumulonimbus clouds, but would be rather invalid for a non-precipitating stage of the clouds). For the green system with lowest precipitation intensities, the slope of the linear least squares fit is negative. As a result of this slope with respect to precipitation rate, it moves
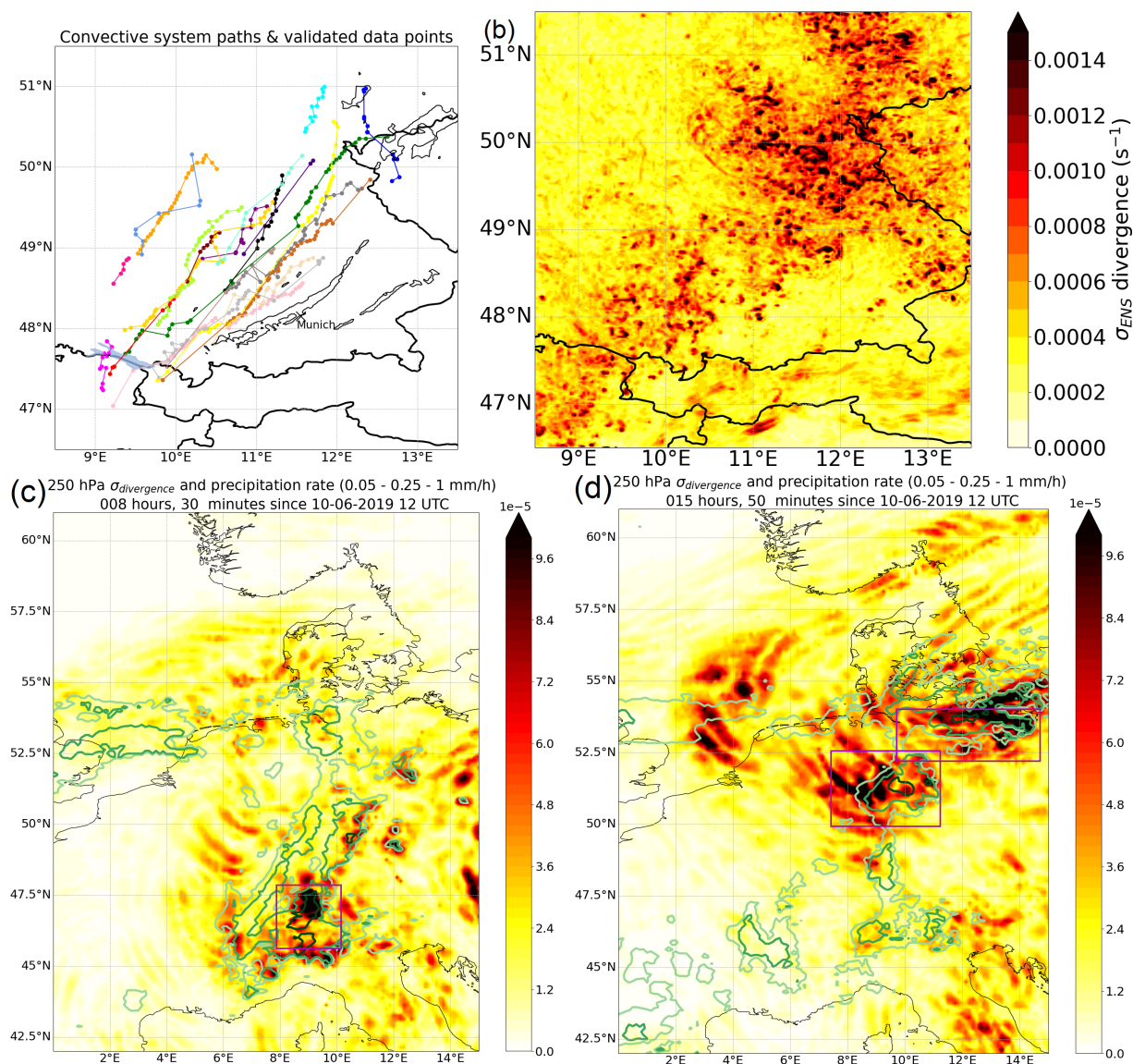
Figure 5. (a) Paths of convective systems over Southern-Germany as included in the dataset of 456 records for ICON PER. In black contours, tracks of observed convective systems with > 55 dBz reflectivity are shown for the same day, which generally appear further to the southeast than those in ICON. The color shading in b-d shows the standard deviation of divergence σ_{ENS}. (b) σ_{ENS} at 255 hPa and the 10th of June 2019 18:00 UTC for ICON-PER. (c,d) σ_{ENS} at 250 hPa and the 10th of June 20:30 (c) (11th of June 3:50 UTC (d)), both for ICON-PAR. Isolines in light green to dark green indicate precipitation intensity over 0.05, 0.25 and 1 mm/h (ensemble mean; bottom plots); the boxes surrounding three convective systems are outlined in purple.
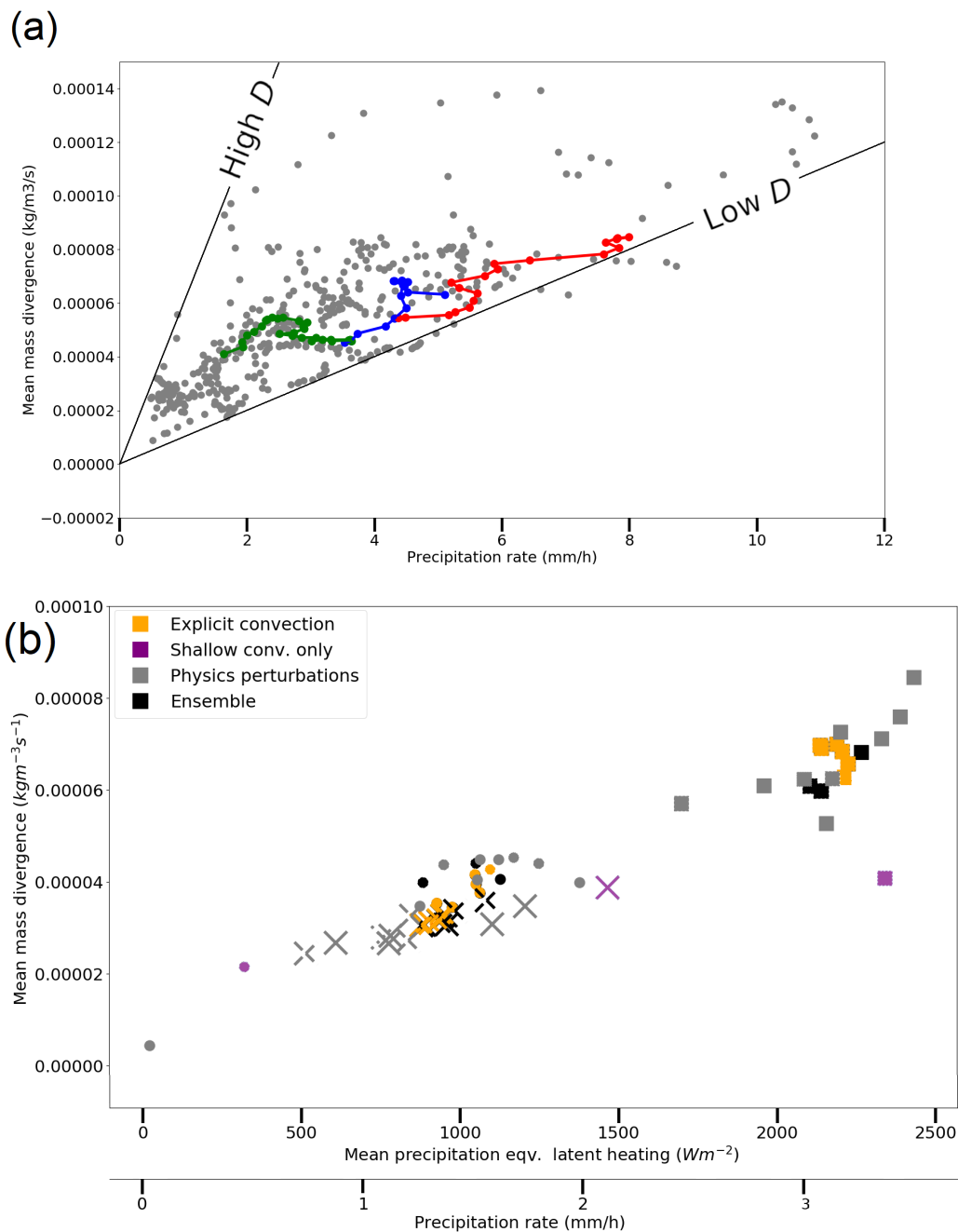
Figure 6. (a) Divergence-latent heating relationship for ICON-PER-simulations in the validated dataset of 456 records (grey), plus the time evolution of three convective systems that form a short squall line in three ensemble members (colors). Divergence is integrated over the 380 to 180 hPa layer. (b) Same relation integrated over model levels from 420-430 hPa up to 175 hPa for ICON-PAR (black: ensemble and parameterisation calls at lower frequencies; grey: perturbed latent heating or convective momentum transport; orange: no deep convective parameterisation; purple: shallow convection parameterisation only). In (b), three different markers correspond to three different convective systems, which correspond to the three purple boxes of Figures 5c and 5d.

(in the diagram) towards a low normalised divergence, while squall line-like structures develop. The other two systems (blue
and red markers) have a positive gradient with respect to precipitation rate, as typical for the background scatter. However, the
intercept of the linear fit at 0 mm/h precipitation rate lies below the intercept value representative of the background fit (see
Table 1 in the Supplement for the intercept and slope parameters of the linear fits). Therefore, these systems are at low D too.
Furthermore, one could see that for the latter two systems the gradient of mass divergence with precipitation rate seems to
decrease, as precipitation rate increases (with time and squall line-like developments). The propagation of these squall line-like
systems towards lower than expected D at a given precipitation rate in Figure 6a fits the expected impact of dimensionality on
convective outflows (Groot and Tost, 2022).

The PAR-simulations, illustrated in Figure 6b and representing three different convective systems as marked with crosses,
squares and dots, suggest a roughly linear relation between mass divergence and net latent heating.If neutral divergence is
assumed in the layer excluded from PER-integration masks, PAR and PER can be compared, even though the integration depth
differs by about 50 hPa between the two. The expected impact, based on an assumption of neutral mass divergence in layers
excluded from the analysis, would translate to a $\approx 25\%$ stronger outflow in PER. Based on the assumption, the corrected mean
PAR-divergence would be higher than the regression line of PER-divergence for a given surface precipitation rate.

Enhanced outflow occurs in PAR compared to PER at given net latent heating rates. The relationship for unperturbed parame-
terised deep convection (black, Figure 6b) appears to be very close to linear, as no information on mode of organisation, such
as the appearance of a squall line structure, is considered with the parameterisation approach (Section 3.2.2). The relationship
is also linear for the ensemble without any convection parameterisation (orange). If only shallow convection is parameterised
(magenta markers), the outflow of one system deviates substantially from the linear relationship, as a result of a downward
shift of outflow levels. Figure 6b suggests that the coarse resolution linearises the precipitation rate-outflow relationship and
that the deviations are generated by cloud-scale dynamical features. Furthermore, physical perturbations in the parameterised
configuration cause slight deviations from the seemingly linear relationship.

Such a behavior agrees well with expectations from the absence of convective organisation in parameterised convection. Explic-
itly resolving deep convection at 13 km grid does not affect the suggested linear relationship. On the other hand, in convection-
permitting simulations at 1 km horizontal grid spacing the latent heating-outflow ratios vary. The envelope of variation is
roughly consistent between ICON PER and idealised CM1 simulations (Groot and Tost, 2022). The study and references
herein indicate that an envelope with variable mass divergence per unit latent heat release is probably the most realistic repre-
sentation.

As there are no systematic patterns of a residual outflow-net latent heating relationship obvious in the PAR simulations, the
analysis of such patterns is restricted to the ICON-PER configuration in Section 6.
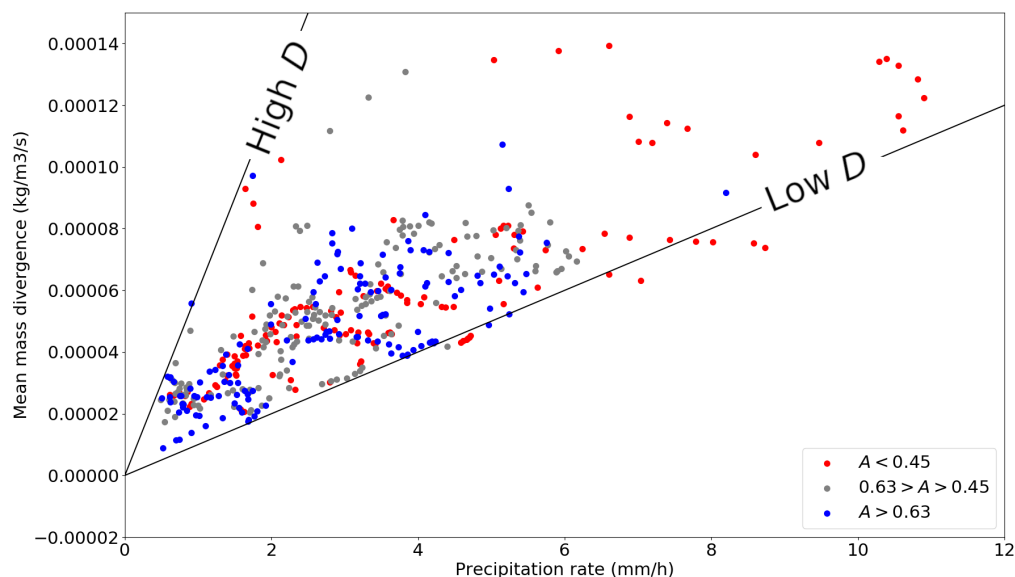
Figure 7. Divergence-precipitation dataset in ICON PER simulations with colors indicating three similarly sized classes of axes ratios. Added are two black lines of constant D: those with 6e-5 $\frac{kg \cdot mm}{m^3 s^1 h^1}$ and 1e-5 $\frac{kg \cdot mm}{m^3 s^1 h^1}$.

6 Dependence of divergent deep convective outflow on properties of convective systems in convection-permitting ICON simulations

6.1 Elongation of convective systems

The elongation of convective systems is quantified by the axis ratio A between the two ellipse axes of the fits to the convective systems. One would expect an on average lower A for systems with a low divergence to precipitation rate ratio D at a given precipitation rate (Groot and Tost, 2022). Furthermore, during the evolution of a convective system A is expected to correlate positively with D. Finally, for two-dimensional convection it is expected that the convective inflow and outflow are mostly parallel to the tropospheric mean winds, resulting in a ellipse orientation O perpendicular to these winds.

Figure 7 suggests that low A corresponds with low D at high precipitation intensities (> 6 mm/h). However, at low precipitation rates the axes ratio classes are more mixed. At low precipitation intensities no clear relationship between A and D is detectable. This suggests that the elongation of convective systems is not the only parameter accountable for anomalies in the outflow strength-latent heating space. The classification into three A-classes can be sensitive to thresholds of A, but Figure 7 shows that sorting of A and D is not supported at low precipitation intensities.

Contrasts are nevertheless present when generating subsets of the simulation data first to all precipitation intensities above 2.5

mm/h and then to two classes of strong D anomalies (at least $\pm 15\%$ from the conditional mean D). Larger D is associated with an average A of 0.602, versus 0.542 for low D. The mean value over the whole dataset is 0.56 with σ of 0.18. Therefore,

370 the difference of the expected sign is significant at 95% confidence. Nevertheless, the difference in A between the classes is lower than expected based on Groot and Tost (2022).

Furthermore, variability in ellipse orientation O within the low D class is strongly reduced compared to instances with high D: $\sigma = 32°$ for low D versus $\sigma = 44°$ for all records and $\sigma = 45°$ degrees for the high D subset. This corresponds to comparatively similar ellipse orientations with reduced variance at low normalised divergence D.

375 ## 6.2 Aggregation of convective systems

Figures 6a and 7 suggest a deviation from the linear relationship towards larger precipitation rate, i.e. reduced D for convective systems with increasing precipitation rates. Therefore, mass divergence is non-linearly related to precipitation rate in the convection-permitting ICON ensemble, in contrast to simulations at coarser resolution (Figure 6b).

A reduction in mass divergence may be caused by the collision of individual three-dimensional outflows from individual cells,

380 as induced by convective aggregation. Hence, convective aggregation may reduce divergence relative to isolated convective cells as more precipitation cells develop within an area. Measures that indicate developing and aggregating convective systems are ellipse area and area over which a precipitation threshold of 10 mm/h is exceeded (Table A1 in the Appendix; Figure 9). Furthermore, precipitation intensity itself generally increases with an increasing number of mature precipitation cells, simultaneously increasing convective aggregation within a respective area.

385 The expected negative correlation of the amount of mass divergence per unit precipitation intensity D with increasing size and (precipitation) intensity of the convective systems is found in the dataset. The most important relation connects precipitation intensity and the ratio D with a correlation coefficient of -0.59 in the fully validated dataset and -0.52 in the larger dataset ($n = 866$). The negative correlation bends off the scatter in Figure 7 towards lower divergences than in case of a continued linear relationship (like in Figure 6b).

390 The robust negative correlation coefficient between D and precipitation rate implies the non-linear behavior within the envelope of Figure 7 is partially predictable: a non-linear best fit between divergence and precipitation rate is expected. A power law with power < 1 could optimally fit the relation between mass divergence and precipitation rates. Indeed, a best fit for the smaller dataset is obtained with an exponent of 0.704. Applying a transform with that power to precipitation rates, the best divergence prediction is obtained in terms of least squares. For the larger dataset, the exponent is 0.606. With bootstrapping the

395 uncertainty in the transformed fit of the smaller dataset is investigated. The 95% confidence of the power transform was estimated at 0.526 to 0.851. However, since multiple highly correlated parameters contribute to the fit (intercept, slope, exponent), the actual parameter uncertainty is likely smaller.

Conditional correlations between the ellipse area and D within precipitation bins also support the signal of convective aggregation. These conditional correlations are summarised in Figure 10: the (sample size) weighted mean correlation coefficient

400 is -0.32, which is significant at 95% confidence. Furthermore, the area > 10 mm/h precipitation rate reveals the same pattern, with a weighted mean correlation coefficient within precipitation bins of -0.29.

The analysis suggests the following evolution of the convective characteristics: increasing precipitation intensity forces a linear increase in mass divergence in the upper troposphere, initially. However, beyond a certain precipitation intensity the mass divergence does not keep up with the initially linear relation anymore. At higher precipitation rates mass divergence tends to grow comparatively slower (i.e. negative feedback). This signal was exemplified by the developing squall line-like structures in Figure 6a. The non-linear divergence reduction is stronger in squall line-like structures than in the average of all sampled convective systems. These convective systems move towards the right lower corner in Figure 6a.

In the supplement (Figure S6) surface-based and mixed/elevated convection subsets are analysed separately, where a fingerprint of convective aggregation is present too. Overall, the non-linearity in mass divergence suggests that the expected impact of convective aggregation on D is present within the PER-dataset. Furthermore, the impact of convective aggregation is qualitatively consistent with idealised LES (Groot and Tost, 2022) .

6.3 Role of convective momentum transport

For the larger dataset with less strict matching criteria, the effect of convective momentum transport on mass divergence has been investigated by normalising both quantities with the precipitation rate (C and D) and analysing conditional correlations of C and D within precipitation rate bins. Thereby, the first order effects of precipitation intensity on mass divergence (Section 6a,b) are filtered out. The precipitation rate bins are constructed such that the ratio between upper and lower bound of the precipitation rate bins is about 4 to 5 and covers the interval 0.6-6.25 mm/h (Figure 10).

Over 11 bins containing 39-150 samples each, the weighted average of the conditional correlation coefficient is 0.31. The equal weight average is 0.34, with exclusively positive correlations up to 0.7-0.8 within bins. Given these statistics, the true correlation coefficient lies probably on the interval 0.2-0.5. Therefore, a small fraction of outflow variability in the convective systems can be explained by variability in CMT (Figure 8).

No single data point with upgradient transport occurs within the dataset (Figure 8a). The sample of 866 records is not fully independent, as only 28 independent convective systems are represented with records at small time lags being correlated. The temporal evolution of several convective systems in a single synoptic environment is of course somewhat biased towards a specific scenario. On the other hand, the coherent background flow supports identifying subtle patterns in the dataset. This contrasts strongly with the experimental method in Groot and Tost (2022) to study CMT effects on mass divergence .

7 Synthesis

7.1 Summary

This study has investigated divergent outflow variability from deep convection in ICON, conditional on the precipitation intensity. Both ensembles of parameterised (PAR; $dx = 13$ km) and explicitly resolved convection (PER; $dx = 1$ km) have been analysed for one event.

Prominent flow variability in the upper troposphere co-locates with convective outflows in both PAR and PER (Figure 5). This
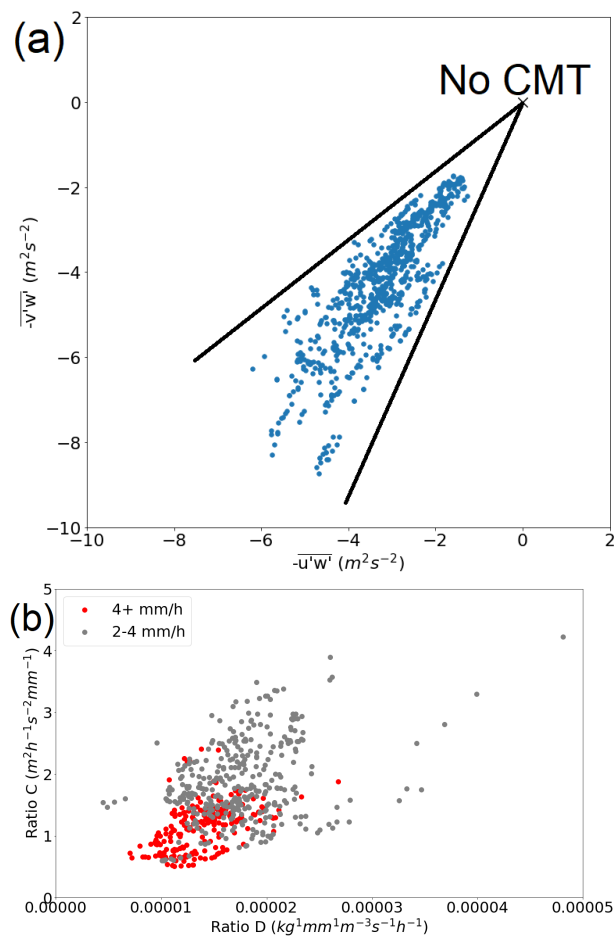
Figure 8. Top (a): two components of the diagnosed vertical CMT integral at 315 hPa (overbar denotes mean operator). Bottom (b): relation between upper-tropospheric mass divergence and the absolute acceleration derived from the CMT diagnostic, both normalised to precipitation rate and for two different classes of precipitation rates (red and grey).
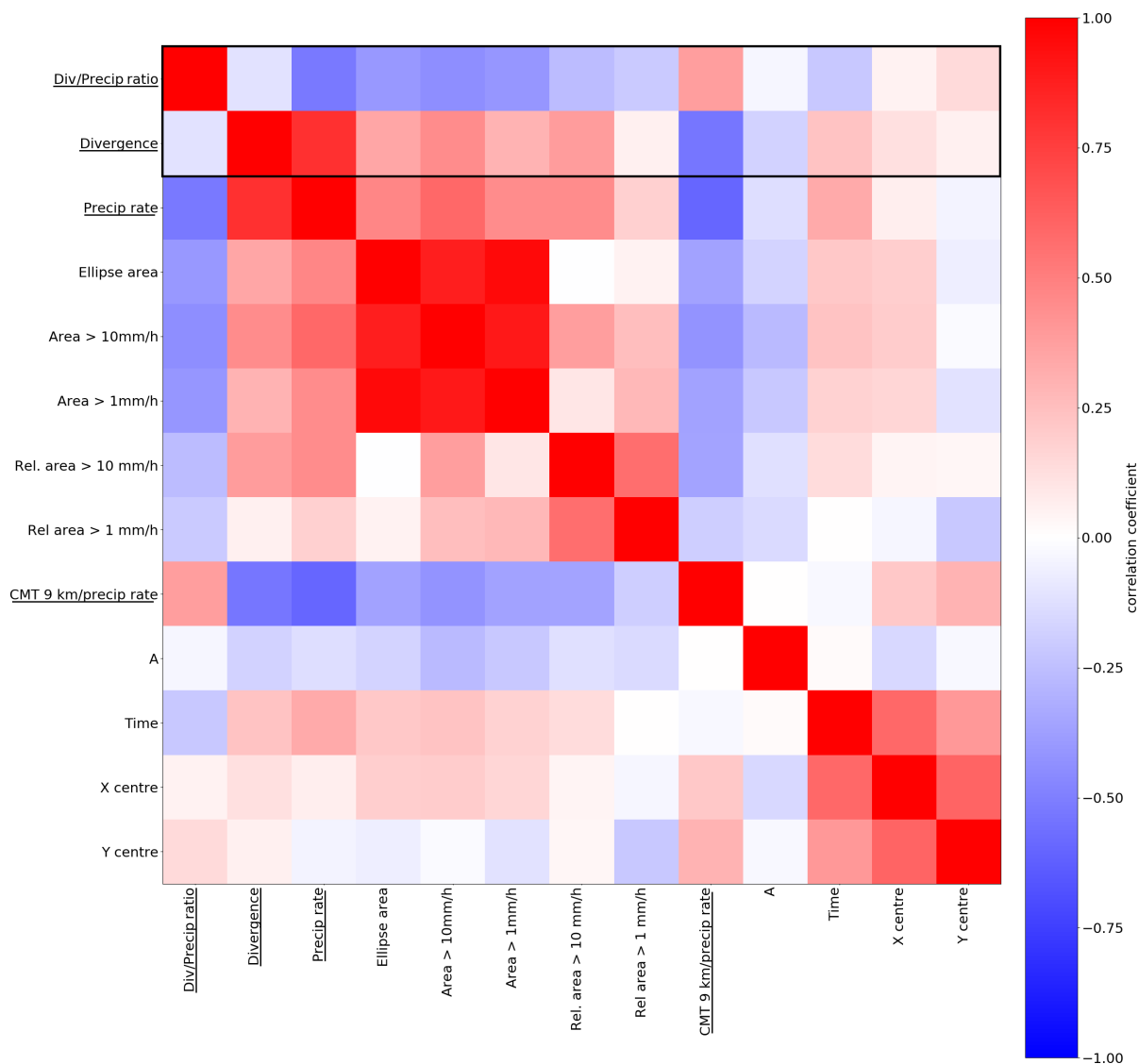
Figure 9. Overview of the correlation structures assessed in Section 6. Underlined variables indicate those that have been derived from the box integration, those without the line indicate variables extracted from ellipse parameters. Based on larger dataset with $n = 866$ samples.
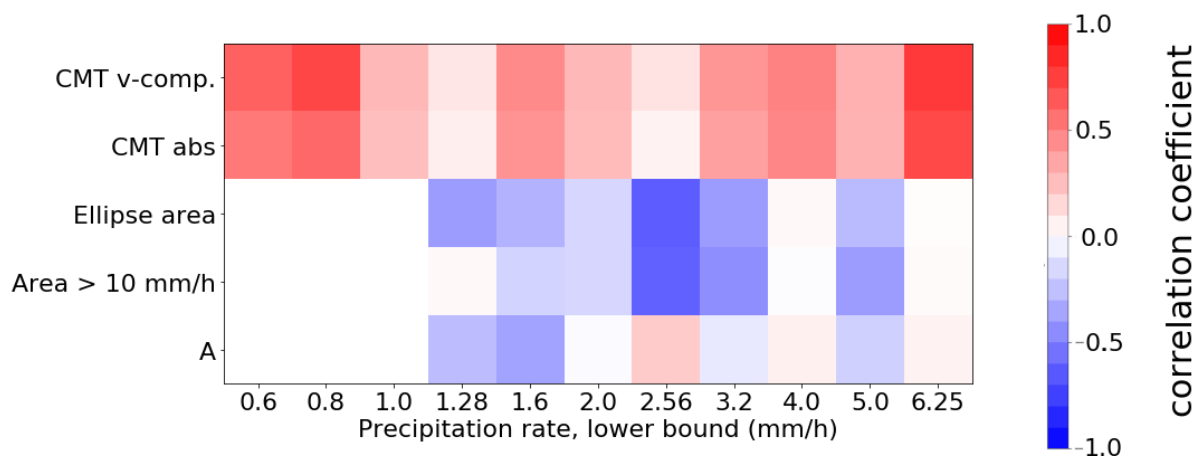
Figure 10. Overview of the correlation structures conditional on precipitation rate as assessed in Section 6. Based on the smaller dataset with $n = 456$ samples. Low precipitation signals are partially omitted due to small sample sizes and weak convection (under 1 mm/h mean precipitation rate over integration box).

analysis suggests that deep convection can be an important source of flow variability in the upper troposphere early in simulations, consistent with Baumgart et al. (2019).

435   PAR-simulations show a highly linear relationship between net latent heating and the outflows with little spread. Conversely, in PER a non-linear relation between precipitation rate and upper-level divergence accompanied by significant scatter away from the mean relationship is found. Even if the precipitation climatology is well represented, the systematic differences between ICON-PAR and ICON-PER implies that the feedback from deep convection to its surroundings at larger scales is likely not accurately represented by parameterised deep convection. The convective flow feedback to larger scales is likely on average overestimated in PAR and using PER ($dx = 1$ km), the representation of outflow variability is improved. An on average overestimated deep convective outflow feedback at given global average precipitation rates may substantially impact regional circulation in weather and climate models. It may contribute to their regional circulation biases.

The convection-permitting simulations have been utilised to explore hypotheses derived from idealised studies (Groot and Tost, 2022) on the impact of convective organisation and aggregation as well as convective momentum transport on upper-tropospheric divergence in real-case simulations.

The first hypothesis states that dimensionality of the outflow (2D versus 3D and, hence, system elongation) affects the magnitude of the convective outflows. Three convective systems developing a squall line-like structure exhibit the expected behaviour over their lifetime: as the squall-line-like-structure develops and precipitation intensity increases, the mass divergence does not necessarily follow. Often, it remains in the lower half of the background distribution of conditional mass divergence. However, in the statistical analysis varied signals have been identified among the expected relations between several ellipse parameters and normalised upper-tropospheric mass divergence D. Therefore, the first hypothesis is not clearly confirmed.

The second hypothesis is that convective aggregation modifies the magnitude of divergent outflows, among systems with sim-

ilar net latent heating rates. This hypothesis can be corroborated by our analysis of the real-case ICON-PER: correlations between outflow magnitude and convective system area and intensity are clearly negative. Furthermore, optimising outflow

455 predictions with a power-transformed precipitation intensity confidently shows sub-linear growth, suggesting a negative feedback as a consequence of convective aggregation and organisation in the dataset.

Finally, the last hypothesis about an absent impact of CMT on the outflows is rejected: conditional correlations within precipitation rate bins reveal that CMT has a small, but significant, impact on the the outflow magnitudes.

7.2 Discussion

460 The applied methods improve insight into the divergent outflow variability in ICON for the studied event, as hypotheses can be investigated. Outflow variability will not collapse onto a linear relationship without variability due to robust effects of convective organisation that have been assessed in a multivariate way. Therefore, this study confirms the results from idealised LES simulations (Groot and Tost, 2022).

7.2.1 Dimensionality hypothesis

465 The dimensionality hypothesis is not strongly supported by our analysis, albeit some indirect evidence points to an impact of dimensionality on divergent outflows. Three suggestions are made, why the dimensionality hypothesis is not strongly supported by the statistics:

- The chosen metric is sub-optimal: it is not able to distinguish nearly-2D and nearly-3D convection well; furthermore, real cases often cannot be unambiguously categorized into the two classes (Trier et al., 1997).

470 - The (elevated) shear profile of this case does not induce sufficient variability in dimensionality of the deep convection

- Opposing statistical patterns compensate each other, even within precipitation bins.

Each of these will be discussed in the following paragraphs one by one. Consequently, the outflow dimensionality seems to contribute only weakly to outflow variability, while the effect of organisation and aggregation is strongly present. Nevertheless, the signal associated with squall line development supports the dimensionality argument, consistently with Bretherton and

475 Smolarkiewicz (1989); Nicholls et al. (1991); Groot and Tost (2022) and others.

The first possibility is that our metric for system dimensionality, namely the ellipse elongation, is not fully adequate, in particular since many convective system in ICON-PER are relatively small. Only few develop clear structures. A solution is to investigate if a poor metric buries the signal by applying the method to a larger set of "PER"-like simulations of various cases. Another solution would be investigating if other algorithms, using a storm-relative flow analysis, could assist the dimension-

480 ality analysis of a wide mixture of organised systems. That may be combined with our method and is achievable (Groot and Tost, 2022; Trier et al., 1997).

Furthermore, the second possibility is that the shear profiles of Groot and Tost (2022) impose a clearer separation between 2D- and 3D-outflow regimes than in our event here. A profile with stronger low-level shear (0-3 km) would enhance squall line

formation and initiate corresponding convection resembling the 2D regime closer. It is worthwhile to revisit the dimensionality
hypothesis with a larger ensemble of convective systems including cases of well-developed squall lines and a (sub-)ensemble
of less strongly organised convection. The development phase of squall lines could be particularly interesting.

Lastly, because of compensating anti-correlation between A and convective aggregation (see Figure 9), a third possibility is
that axis ratio A hides the direct dimensionality signal in the outflow variability. The signal may even be hidden if conditional
correlations within precipitation rate bins are considered (Figure 10). This is possible if A is a sub-optimal proxy for the di-
mensionality of convective outflows. Two correlation effects within precipitation bins could oppose another, namely convective
aggregation and A as a proxy for outflow dimensionality. Consequently, analysed patterns may seemingly be explained by ag-
gregation only, even if the dimensionality hypothesis explains a substantial proportion of the examined outflow variability.
Nevertheless, if the dimensionality and aggregation hypotheses are strongly interrelated, as suggested in Groot and Tost (2022),
it would be surprising if a compensation between the correlation signals would occur. The dimensionality hypothesis should
probably be easier to prove than the aggregation hypothesis. Therefore, a follow-up study with a squall line ensemble versus
less strongly organised deep convection is needed to resolve this possible paradox.

7.2.2 CMT hypothesis

The impact of CMT on the outflows is found to be much more pronounced here than in the LES of Groot and Tost (2022).
CMT was not found to (directly) affect the convective outflows in the LES-simulations, possibly because the imposed shear
layer was too shallow. Upper-tropospheric wind shear was completely absent in that configuration, whereas any real world
has non-zero shear in the upper troposphere. In the LES-simulations, the shallow shear configuration was used to reduce cell
propagation through the small domain. Shallow shear configurations can reduce the average height that parcels in convective
cells reach (Coniglio et al., 2006) and the associated reduced vertical overturning suppresses the interaction between the shear
layer and the divergent outflows (in agreement with Brown (1999). Therefore, the impact of CMT on the outflows is likely
suppressed in Groot and Tost (2022).

Additionally, the ICON-PER configuration is arguably most suitable for detecting subtle (reasonable, real case) CMT impacts
on the divergent outflows. Conversely, the setup does not allow in-depth understanding of the mechanisms behind outflow
variability due to the complexity of scenario and the amplitude of the systems in close spatio-temporal proximity. Additional
LES-experiments targeting CMT could enhance insight in future studies.

7.2.3 Further research

To summarise, this study shows further investigation is needed to thoroughly understand the role of dimensionality for the
magnitude of divergent outflows in a practical NWP-setting. Furthermore, convective organisation and aggregation are found
to be key players for the magnitude of divergent outflows in practice, which is only accounted for by convection-permitting
simulations at 1 km horizontal grid spacing.

7.3 Implications

515

This work once more confirms the strong link between precipitation variability and flow variability in an ensemble. This close connection may lead to perturbation growth in a forecast or spread in an ensemble. The downstream propagation of perturbations is not directly addressed here. Nevertheless, the divergence variability (Figure 5) suggests a potential role for divergent outflows propagating precipitation variability and other convective variability (e.g. CMT) to large-scale dynamics. The poten-

520 tial downstream impact of convective variability via this (and other) mechanisms is addressed by e.g., Baumgart et al. (2019) and Rodwell et al. (2013). Furthermore, this work suggests that the convective contribution to flow variability can be separated into a component of precipitation variability and another component of superposed conditional divergence variability (D variability), induced by convective organisation and aggregation. This role of convective organisation may relate to the results of Rodwell et al. (2013). Despite, a separate examination in an event with upscale impact of the convection is needed to assess

525 mechanisms acting.

The separation of divergence variability into the above mentioned components has significance for weather and climate modelling. Only the former component can be modelled with regular deep convection parameterisation schemes. The latter component is (nearly) absent in parameterised configurations, but is accounted for in a convection-permitting setup. Assessing convective variability, conditioning deep convective variability on precipitation rate is an important tool to illustrate the two

530 components of variability. Thereby, the feedback between deep convection and its environment is discerned. Common variability associated with both precipitation rate and upper-tropospheric dynamics within convective systems has been discussed in Groot and Tost (2023, 2022).

Based on the second and to a lesser extent third hypothesis of this work, convective organisation and aggregation affect dynamics. Therefore, it is needed to include these factors into error growth studies, assisting them to extend all the way from the

535 convective to the planetary scales. Consequently, the conditional convective perspective shaped here can be connected with the Baumgart et al. (2019)-perspective.

8 Conclusions

The multivariate exploration of divergent outflows of deep moist convection in real case weather prediction shows that their dependency is rather complex and cannot easily be distinguished and assigned to individual processes. However, major variability

540 of the relationship of precipitation and upper-tropospheric divergent outflow is explained by effects that were also present in LES-analyses (Groot and Tost, 2022). The following can be concluded on variability in upper-tropospheric divergent outflows from deep convection ("this outflow"):

– The outflow is responsible for major ensemble spread in the divergent part of the upper-tropospheric wind during a convective event.

545 – Convection-permitting (1 km horizontal grid spacing) represent the effect of aggregation on divergent outflow from deep convection and an envelope of divergent outflow exists at a given net latent heating rate.

- Using simulations at coarser resolution probably implies assuming a (near-)linear relationship between the outflow and net latent heating.

- Indications exist showing that the fingerprint of dimensionality is represented in variability of this outflow in ICON convection-permitting settings, but a case study comparing squall lines that highly resemble 2D-convection with less organised convection is needed to increase the confidence in this finding.

- Convective momentum transport seems to weakly affect this outflow directly.

- To understand convectively induced flow perturbations better, a separation into two components of convective variability is necessary: 1. variability in predicted mesoscale precipitation rates; 2. representation of the residual (conditional) flow perturbations, which depend on the cloud-scale dynamics.

Code and data availability. The code used in this work and the output for one PER and one PAR simulation are available in Groot and Kuntze (2023) (last accessed: 16-02-2023).

Appendix A: Table of parameters in ellipse dataset

Table A1. List of parameters in the dataset of ellipse records, with their descriptions.

Name of parameter	Unit	Explanation (if necessary)	Symbol
Ellipse id	#	Each ellipse comes with an id	
Time stamp	# 5 min	Each corresponding output time step has a time stamp	
Axis ratio	-	Ratio between major and minor axis of ellipse	A
Mean precipitation rate	mm/h	Mean surface precipitation rate over convective system's track following box	
Mean mass divergence	$\frac{kg}{m^3 s}$	Mean upper tropospheric (380-180 hPa) mass divergence rate over convective system's track following box	
Div/precip ratio	$\frac{kg \cdot mm}{m^3 s^1 h^1}$	Ratio between box mean mass divergence and box mean precipitation rate	D
U-component of CMT eddy flux	$m^2 s^{-2}$	Mean value of $u'w'$ at model level 25, about 315 hPa, where $'$ indicates domain average relative velocity perturbations	
V-component of CMT eddy flux	$m^2 s^{-2}$	Mean value of $v'w'$ at model level 25, about 315 hPa	
Absolute vertical integral of CMT acceleration	$m^2 s^{-2}$	Mean value of $[(u'w')^2 + (v'w')^2]^{\frac{1}{2}}$ at model level 25, about 315 hPa	
Ratio absolute integral of CMT acceleration over precip rate	$\frac{m^2 h}{s^2 mm^1}$	As above, but relative to precipitation rate in mm/h (also computed for U and V component separately)	C
Xcentre	grid cell #	Centre of the fitted ellipse in zonal direction	
Ycentre	grid cell #	Centre of the fitted ellipse in meridional direction	
Ellipse angle/orientation	°	Orientation of the major axis of the ellipse with respect to a reference direction	O
Major axis length	km		
Minor axis length	km		
Ellipse area	# grid cell^2	Area of the ellipse that has been fit, can be converted to square km (1 grid cell is approximately 4 km^2)	
Mean precipitation rate over ellipse	mm/h	Mean precipitation rate over ellipse only	
Area >10 mm/h precipitation rate	-	Fraction of ellipse exceeding 10 mm/h ("convective") precipitation	
Area >1 mm/h precipitation rate	-	Fraction of ellipse exceeding 1 mm/h ("stratiform + convective") precipitation	
X distance ellipse and box centre	km	Distance between box centre and fitted ellipse in x-direction	
Y distance ellipse and box centre	km	Distance between box centre and fitted ellipse in y-direction	
Total distance ellipse/box	km	Total distance obtained from its x- and y-component	

Author contributions. EG (ICON-PAR) and PK (ICON-PER) carried out the simulations for this work, under the supervision of HT and AM.

560   EG designed the study, developed the ellipse fitting algorithm, carried out the analysis and wrote the manuscript with contributions from all co-authors.

Competing interests. The authors have no competing interests to declare.

Acknowledgements. The research leading to these results has been done within the subprojects 'A1 - Multiscale analysis of the evolution of forecast uncertainty' and 'B1 - Microphysical uncertainties in hailstorms using statistical emulation and stochastic cloud physics' of the

565   Transregional Collaborative Research Center SFB / TRR 165 'Waves to Weather' funded by the German Research Foundation (DFG). The authors would also like to acknowledge the computing time granted on the supercomputer MOGON 2 at Johannes Gutenberg-University Mainz (hpc.uni-mainz.de, last accessed: 02-02-2023).

References

Arakawa, A.: The Cumulus Parameterization Problem: Past, Present, and Future, JOURNAL OF CLIMATE, 17, 2493–2525, 2004.

Baumgart, M., Ghinassi, P., Wirth, V., Selz, T., Craig, G. C., and Riemer, M.: Quantitative View on the Processes Governing the Up-scale Error Growth up to the Planetary Scale Using a Stochastic Convection Scheme, Monthly Weather Review, 147, 1713–1731, https://doi.org/10.1175/mwr-d-18-0292.1, 2019.

Bechtold, P., Semane, N., Lopez, P., Chaboureau, J., Beljaars, A., and Bormann, N.: Representing equilibrium and nonequilibrium convection in large-scale models, Journal of the Atmospheric Sciences, 71, 734–753, 2014.

Bretherton, C. S. and Smolarkiewicz, P. K.: Gravity Waves, Compensating Subsidence and Detrainment around Cumulus Clouds, Journal of Atmospheric Sciences, 46, 740 – 759, https://doi.org/10.1175/1520-0469(1989)046<0740:GWCSAD>2.0.CO;2, 1989.

Brown, A.: Large-eddy simulation and parametrization of the effects of shear on shallow cumulus convection, Boundary-layer meteorology, 91, 65–80, 1999.

Clarke, S., Gray, S., and Roberts, N.: Downstream influence of mesoscale convective systems. Part 1: influence on forecast evolution, Quarterly Journal of the Royal Meteorological Society, 145, 2933–2952, https://doi.org/https://doi.org/10.1002/qj.3593, 2019a.

Clarke, S., Gray, S., and Roberts, N.: Downstream influence of mesoscale convective systems. Part 2: Influence on ensemble forecast skill and spread, Quarterly Journal of the Royal Meteorological Society, 145, 2953–2972, https://doi.org/https://doi.org/10.1002/qj.3613, 2019b.

Coniglio, M. C., Stensrud, D. J., and Wicker, L. J.: Effects of upper-level shear on the structure and maintenance of strong quasi-linear mesoscale convective systems, Journal of the Atmospheric Sciences, 63, 1231–1252, https://doi.org/10.1175/jas3681.1, 2006.

Done, J. M., Craig, G. C., Gray, S. L., Clark, P. A., and Gray, M. E. B.: Mesoscale simulations of organized convection: Importance of convective equilibrium, Quarterly Journal of the Royal Meteorological Society, 132, 737–756, https://doi.org/https://doi.org/10.1256/qj.04.84, 2006.

Durran, D. and Gingrich, M.: Atmospheric Predictability: Why Butterflies Are Not of Practical Importance, Journal of the Atmospheric Sciences, 71, 2476 – 2488, https://doi.org/10.1175/JAS-D-14-0007.1, 2014.

Giorgetta, M., Brokopf, R., Crueger, T., Esch, M., Fiedler, S., Helmert, J., Hohenegger, C., Kornblueh, L., Köhler, M., Manzini, E., et al.: ICON-A, the atmosphere component of the ICON earth system model: I. Model description, Journal of Advances in Modeling Earth Systems, 10, 1613–1637, 2018.

Grant, L. D., Moncrieff, M. W., Lane, T. P., and van den Heever, S. C.: Shear-parallel tropical convective systems: Importance of cold pools and wind shear, Geophysical Research Letters, 47, e2020GL087 720, 2020.

Groot, E. and Kuntze, P.: Dataset of "Divergent convective outflow in ICON deep convection permitting and parameterised deep convection simulations": sample simulations, https://doi.org/10.5281/zenodo.7541630, Funded by TRR-165 (DFG): 'Wavestoweather' (see wavestoweather.de), 2023.

Groot, E. and Tost, H.: Divergent convective outflow in large eddy simulations, EGUsphere, pp. 1–25, https://doi.org/https://doi.org/10.5194/egusphere-2022-1261, 2022.

Groot, E. and Tost, H.: Evolution of squall line variability and error growth in an ensemble of large eddy simulations, Atmospheric Chemistry and Physics, 23, 565–585, https://doi.org/https://doi.org/10.5194/acp-23-565-2023, 2023.

Judt, F.: Atmospheric Predictability of the Tropics, Middle Latitudes, and Polar Regions Explored through Global Storm-Resolving Simulations, Journal of the Atmospheric Sciences, 77, 257 – 276, https://doi.org/10.1175/JAS-D-19-0116.1, 2020.

Keane, R. J., Craig, G., Keil, C., and Zängl, G.: The Plant–Craig Stochastic Convection Scheme in ICON and Its Scale Adaptivity, Journal of the Atmospheric Sciences, 71, 3404–3415, https://journals.ametsoc.org/doi/abs/10.1175/JAS-D-13-0331.1, 2014.

Lawrence, M. and Salzmann, M.: On interpreting studies of tracer transport by deep cumulus convection and its effects on atmospheric chemistry, Atmospheric Chemistry and Physics, 8, 6037–6050, 2008.

Lorenz, E.: The predictability of a flow which possesses many scales of motion, Tellus, 21, 289–307, https://doi.org/10.3402/tellusa.v21i3.10086, 1969.

Mapes, B. E.: Gregarious Tropical Convection, Journal of Atmospheric Sciences, 50, 2026 – 2037, https://doi.org/10.1175/1520-0469(1993)050<2026:GTC>2.0.CO;2, 1993.

Mapes, B. E. and Houze, R. A.: Diabatic Divergence Profiles in Western Pacific Mesoscale Convective Systems, Journal of Atmospheric Sciences, 52, 1807 – 1828, https://doi.org/10.1175/1520-0469(1995)052<1807:DDPIWP>2.0.CO;2, 1995.

Matsunobu, T., Keil, C., and Barthlott, C.: The impact of microphysical uncertainty conditional on initial and boundary condition uncertainty under varying synoptic control, Weather and Climate Dynamics, 3, 1273–1289, https://doi.org/10.5194/wcd-3-1273-2022, 2022.

Nicholls, M. E., Pielke, R. A., and Cotton, W. R.: Thermally Forced Gravity Waves in an Atmosphere at Rest, Journal of Atmospheric Sciences, 48, 1869 – 1884, https://doi.org/10.1175/1520-0469(1991)048<1869:TFGWIA>2.0.CO;2, 1991.

Prill, F., Reinert, D., Rieger, D., and Zängl, G.: ICON Model Tutorial 2020, Availableathttps://www.dwd.de/DE/leistungen/nwv_icon_tutorial/pdf_einzelbaende/icon_tutorial2020.pdf, 2020.

Rodwell, M. J., Magnusson, L., Bauer, P., Bechtold, P., Bonavita, M., Cardinali, C., Diamantakis, M., Earnshaw, P., Garcia-Mendez, A., Isaksen, L., Källén, E., Klocke, D., Lopez, P., McNally, T., Persson, A., Prates, F., and Wedi, N.: Characteristics of Occasional Poor Medium-Range Weather Forecasts for Europe, Bulletin of the American Meteorological Society, 94, 1393–1405, https://doi.org/10.1175/bams-d-12-00099.1, 2013.

Satoh, M., Stevens, B., Judt, F., Khairoutdinov, M., Lin, S., Putman, W., and Düben, P.: Global cloud-resolving models, Current Climate Change Reports, 5, 172–184, 2019.

Seifert, A.: A revised cloud microphysical parameterization for COSMO-LME, COSMO Newsletter, 7, 25–28, 2008.

Seifert, A. and Beheng, K.: A two-moment cloud microphysics parameterization for mixed-phase clouds. Part 1: Model description, Meteorology and atmospheric physics, 92, 45–66, 2006.

Selz, T. and Craig, G. C.: Upscale Error Growth in a High-Resolution Simulation of a Summertime Weather Event over Europe, Monthly Weather Review, 143, 813–827, https://doi.org/10.1175/mwr-d-14-00140.1, 2015a.

Selz, T. and Craig, G. C.: Simulation of upscale error growth with a stochastic convection scheme, Geophysical Research Letters, 42, 3056–3062, https://doi.org/10.1002/2015gl063525, 2015b.

Selz, T., Riemer, M., and Craig, G.: The transition from practical to intrinsic predictability of midlatitude weather, Journal of the Atmospheric Sciences, https://doi.org/10.1175/JAS-D-21-0271.1, 2022.

Tiedtke, M.: A comprehensive mass flux scheme for cumulus parameterization in large-scale models, Monthly weather review, 117, 1779–1800, 1989.

Trier, S. B., Skamarock, W. C., and LeMone, M. A.: Structure and Evolution of the 22 February 1993 TOGA COARE Squall Line: Organization Mechanisms Inferred from Numerical Simulation, Journal of the Atmospheric Sciences, 54, 386 – 407, https://doi.org/10.1175/1520-0469(1997)054<0386:SAEOTF>2.0.CO;2, 1997.

Wilhelm, J., Mohr, S., Punge, H. J., Mühr, B., Schmidberger, M., Daniell, J. E., Bedka, K. M., and Kunz, M.: Severe thunderstorms with large hail across Germany in June 2019, Weather, 76, 228–237, https://doi.org/https://doi.org/10.1002/wea.3886, 2021.

Zängl, G., Reinert, D., Rípodas, P., and Baldauf, M.: The ICON (ICOsahedral Non-hydrostatic) modelling framework of DWD and MPI-M: Description of the non-hydrostatic dynamical core, Quarterly Journal of the Royal Meteorological Society, 141, 563–579, 2015.

Zhang, F.: Dynamics and structure of mesoscale error covariance of a winter cyclone estimated through short-range ensemble forecasts, AMETSOC, https://doi.org/10.1175/MWR3009.1, 2005.

Zhang, F., Bei, N., Rotunno, R., Snyder, C., and Epifanio, C. C.: Mesoscale Predictability of Moist Baroclinic Waves: Convection-Permitting Experiments and Multistage Error Growth Dynamics, Journal of the Atmospheric Sciences, 64, 3579–3594, https://doi.org/10.1175/jas4028.1, 2007.

Zhang, F., Sun, Y., Magnusson, L., Buizza, R., Lin, S., Chen, J., and Emanuel, K.: What Is the Predictability Limit of Midlatitude Weather?, Journal of the Atmospheric Sciences, 76, 1077 – 1091, https://doi.org/10.1175/JAS-D-18-0269.1, 2019.